RESEARCH ARTICLE

JENER Journal of Empirical and Non-Empirical Research
Volume 2, Issue 5, Page 563-570 | Article No. 68
DOI: 10.4898/jener.v2i5.a68
ISSN: 7895-9216
Journal homepage: https://jenerjournal.com
Journal email: editor@jenerjournal.com

JENER Journal
JENER Journal of Empirical and Non-Empirical Research

Design and Modeling of a Mobile Robotic Solar Tracking System

Yelebe, S. Robert[1] & Newton I. Agbeboh[2]

[1,2]Department of Mechanical and Mechatronics Engineering, Federal University Otuoke, Nigeria

ARTICLE INFORMATION

Article history:
Published: 24 May 2026

Keywords:
Solar Tracker
Mobile Robotic System
Photovoltaic
Structural Analysis
Chain Drive
Arduino
LDR Sensor

ABSTRACT

This paper presents the design, structural modeling, and mechanical analysis of a mobile robotic solar tracking system intended to maximize photovoltaic energy harvest while enhancing accessibility and deployability for small-scale users in rural and urban environments. The system integrates a monocrystalline silicon solar panel, a 12 V/350 W DC motor for azimuth rotation, a stepper motor for precision elevation control, Light-Dependent Resistor (LDR) sensors for irradiance gradient detection, a mobile caster-wheel base for repositioning, and an Arduino-based control architecture. Key mechanical parameters include; frame bending stress, mass moment of inertia, wind loading, motor torque, and chain-drive transmission capacity, were analytically derived and validated against material strength limits. Frame bending stress was 103.97 N/m², well within the 270 MPa yield limit of 6061-T6 aluminium; motor torque of 1.114 N·m was sufficient for continuous azimuth tracking; and a chain drive factor of safety of 2,120 confirmed substantial transmission margins. The hybrid control architecture combining open-loop sun-path algorithms with closed-loop.

1. Introduction

The rising global demand for clean energy has positioned solar photovoltaic (PV) technology as a central pillar of sustainable electricity generation. However, conventional fixed-tilt solar panels often fail to maximize energy capture because they cannot follow the sun's continuous movement throughout the day and across seasons (Sadeghi et al., 2025). The global transition toward low-carbon electricity has therefore intensified research into solar tracking systems that automatically adjust panel orientation to optimize solar irradiance reception.

Solar tracking systems consistently deliver notable performance improvements. Single-axis trackers typically generate 15–35% more annual energy than fixed installations, while dual-axis systems can achieve gains of 30–45% or higher depending on geographical location and climatic conditions (Paliyal, 2024; Liang et al., 2019). A 360-degree azimuth capability is particularly valuable in equatorial and mid-latitude regions, where the sun traces a wide east–west arc and local obstructions may place the sun behind a tracker constrained to less than full rotation (Shufat et al., 2019; Wan et al., 2020). Full azimuth rotation eliminates mechanical dead zones, enabling optimal alignment under atypical sky conditions and complex urban site layouts.

Despite these benefits, traditional solar trackers often remain inaccessible to small-scale users in rural environments. Many existing systems are large, expensive, and designed for permanent installation, requiring significant civil works and technical expertise. Their lack of mobility also creates challenges in areas where seasonal relocation becomes necessary due to changing land use or vegetation patterns (Kamela, 2024; Toginho, 2020). Recent developments have therefore explored the integration of robotic technologies with solar tracking, enabling platforms to reposition themselves to locations with better solar exposure while continuously adjusting panel orientation (Al-Turki & Qamber, 2019; Jiang et al., 2024).

Modern trackers employ open-loop astronomical algorithms, closed-loop irradiance-gradient sensing, or hybrid combinations of both. Hybrid schemes have demonstrated pointing errors as low as ±0.5° and improved robustness under variable sky conditions (Al-Nimr et al., 2018; Wan et al., 2020). Despite this body of work, the systematic integration of full 360-degree azimuth rotation, robust elevation control, lightweight robotic mobility, and intelligent sensor fusion into a single scalable platform has received limited attention (Paliyal, 2024; Mohanta et al., 2024).

The aim of this study is to design a mobile robotic solar tracking system with a focus on improving accessibility and deployability for small-scale users. Three specific objectives were pursued: (i) to carry out a systematic mechanical and structural design of the robotic solar tracking platform; (ii) to analyze the stresses of the aluminium frame; and (iii) to assess wind loading and drivetrain sizing to ensure structural adequacy and reliable continuous outdoor operation.

2. Literature Review

Sumathi et al. (2017) conducted a comprehensive review of solar tracking systems and concluded that dual-axis trackers consistently outperform single-axis and fixed-tilt configurations in terms of annual energy yield. The authors noted that hybrid control strategies, combining astronomical models with real-time irradiance feedback offers the most favourable balance between pointing precision and adaptability across weather conditions.

Wan et al. (2017) reported experimental findings from a field-deployed automated dual-axis tracking system that achieved approximately 26.9% more power generation than a fixed-tilt reference array under clear-sky conditions, retaining a 12.8%

advantage under heavy overcast. Their study identified actuator wear as the primary long-term reliability concern and recommended gear-reduced drive configurations to lower torque demand at the motor shaft.

Awasthi et al. (2020) performed a systematic review identifying 25–40% as the energy gain attributable to dual-axis tracking relative to fixed-tilt baselines, consistent with diverse climatic and geographic conditions. Mahmood et al. (2020) demonstrated that microcontroller-driven electromechanical trackers constructed from commercially available components can achieve tracking accuracies comparable to industrial systems at significantly reduced cost, confirming the feasibility of the proposed design approach for small-scale commercial and rural applications.

On the structural side, Rahal (2026) employed finite element analysis to evaluate stress distributions under various loading conditions for a dual-axis tracker, while Valentín et al. (2022) investigated tracker failure due to wind-induced effects, underscoring the importance of proper drivetrain sizing and structural evaluation. Kamela (2024) specifically addressed wind load analysis for a dual-axis stand-alone PV structure, confirming that aerodynamic assessment is critical for field-deployed systems. Lazaroiu et al. (2023) further demonstrated that mobile or relocatable solar platforms can serve as distributed energy resources, supporting flexible urban and rural deployment strategies.

3. System Overview and Component Selection

The proposed system adopts an azimuth–altitude configuration in which the base rotates through a full 360-degree azimuth arc while a secondary elevation joint controls the panel tilt angle. The overall architecture comprises a solar panel sub-system, an energy storage and conditioning sub-system, a mechanical drivetrain, and an embedded control layer. A mobile caster-wheel base enables the platform to be repositioned to locations with better solar exposure without requiring permanent foundations, distinguishing this design from conventional industrial trackers.

Component selection was governed by electrical performance, mechanical durability, thermal stability, and compatibility with the Arduino-based control architecture, see Figure 1. The monocrystalline silicon panel was chosen for its high conversion efficiency and stable temperature coefficient. Lithium-ion batteries buffer PV output for continuous motor operation. LDR sensors fabricated from cadmium sulfide (CdS) deliver fast, low-cost irradiance gradient detection for closed-loop sun tracking. The azimuth axis employs a 12 V/350 W DC motor, while a stepper motor provides precision elevation adjustments. Table 1 summarises all primary components, their materials, functional roles, and selection criteria.

Table 1. Component Materials, Functions, and Selection Criteria for the Mobile Robotic Solar Tracking System

No.	Component	Material	Function	Selection Criteria
1	Solar Panel	Monocrystalline silicon	Converts solar irradiance to electrical energy	High efficiency; good temperature coefficient; long lifespan
2	Battery	Lithium-ion	Stores electrical energy for load supply	High energy density; long cycle life; low self-discharge
3	Booster	Copper and FR4 PCB	Steps up voltage to operating levels	High conductivity; thermal stability; compact
4	Arduino Microcontroller	FR4 fibreglass PCB	Logic control, sun-tracking algorithm, actuation	Electrical insulation; heat resistance; lightweight
5	LDR Sensors	Cadmium Sulfide (CdS)	Detects irradiance gradient for sun sensing	High sensitivity; fast response; compact
6	DC Motor	Copper windings; steel housing	Provides rotary motion for azimuth axis	High torque; durable; efficient
7	Stepper Motor	Copper windings; steel rotor	Precise angular stepping for elevation axis	High torque; precision stepping; controller compatible
8	Charge Controller	FR4 PCB; plastic casing	Regulates power flow from panel to battery	Efficient charge control; overcharge protection
9	Solar Inverter	Aluminium casing; silicon chips	Converts DC output to AC supply	High conversion efficiency; thermal management
10	Caster Wheels	Polyurethane; steel frame	Supports base movement and rotation	High load capacity; wear resistance; smooth rolling

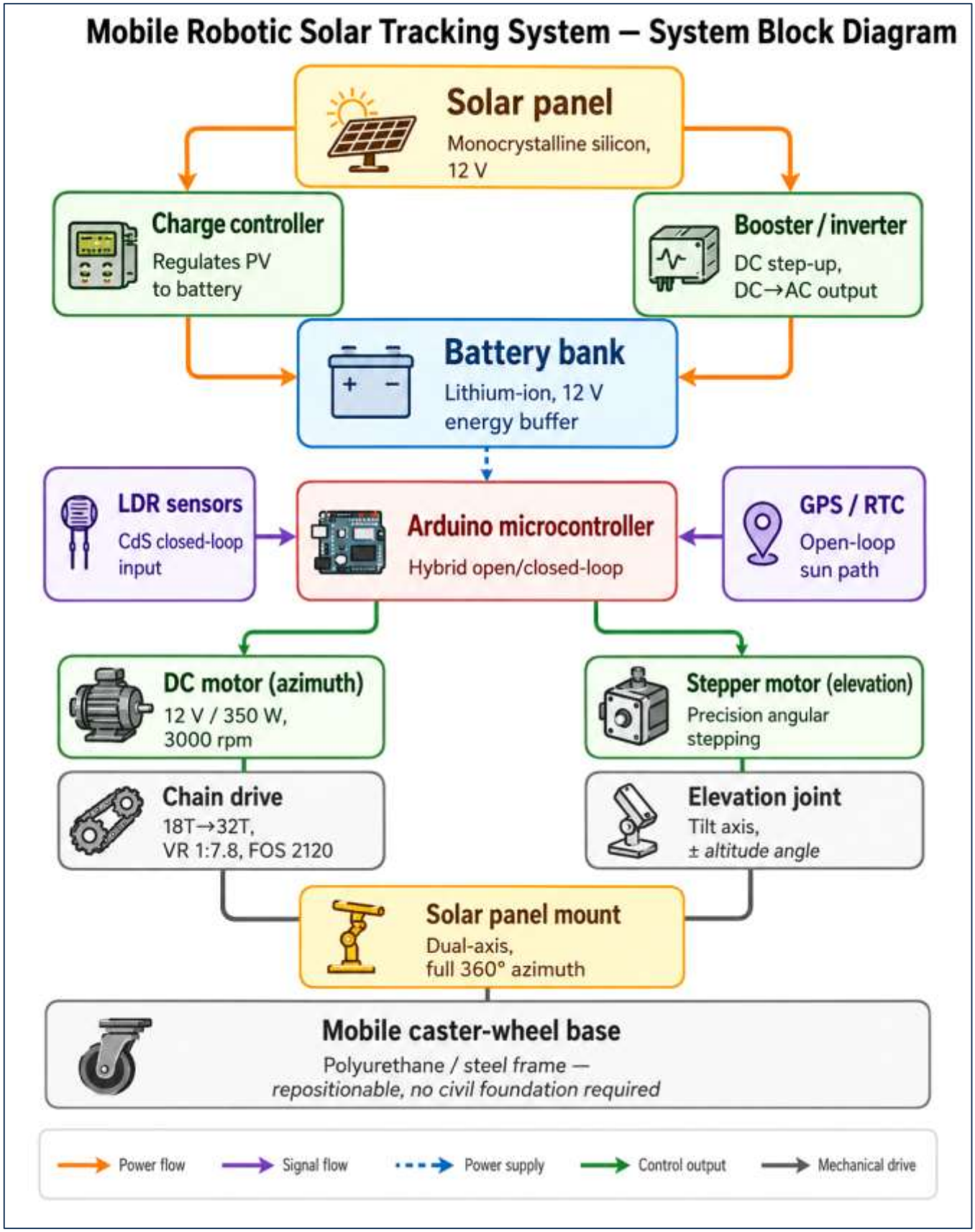

Figure 1: System block diagram of the mobile robotic solar tracking system

4. Design Calculations and Structural Analysis

The following subsections present the analytical derivations that establish the structural adequacy and mechanical performance of the system. All calculations are based on the dead-load inventory and the electrical ratings of the drive motor. Advanced modeling techniques such as finite element analysis complement these analytical methods in evaluating stress distributions under various loading conditions, including self-weight, panel weight, and dynamic forces during movement (Rahal, 2026; Hubach, 2019).

Figure 2, presents design drawing of the mobile robotic solar tracking system, upon which the stress analysis of the frame, mass moment of inertia, structural integrity, wind loading, motor and drive design parameters and considerations are determined.

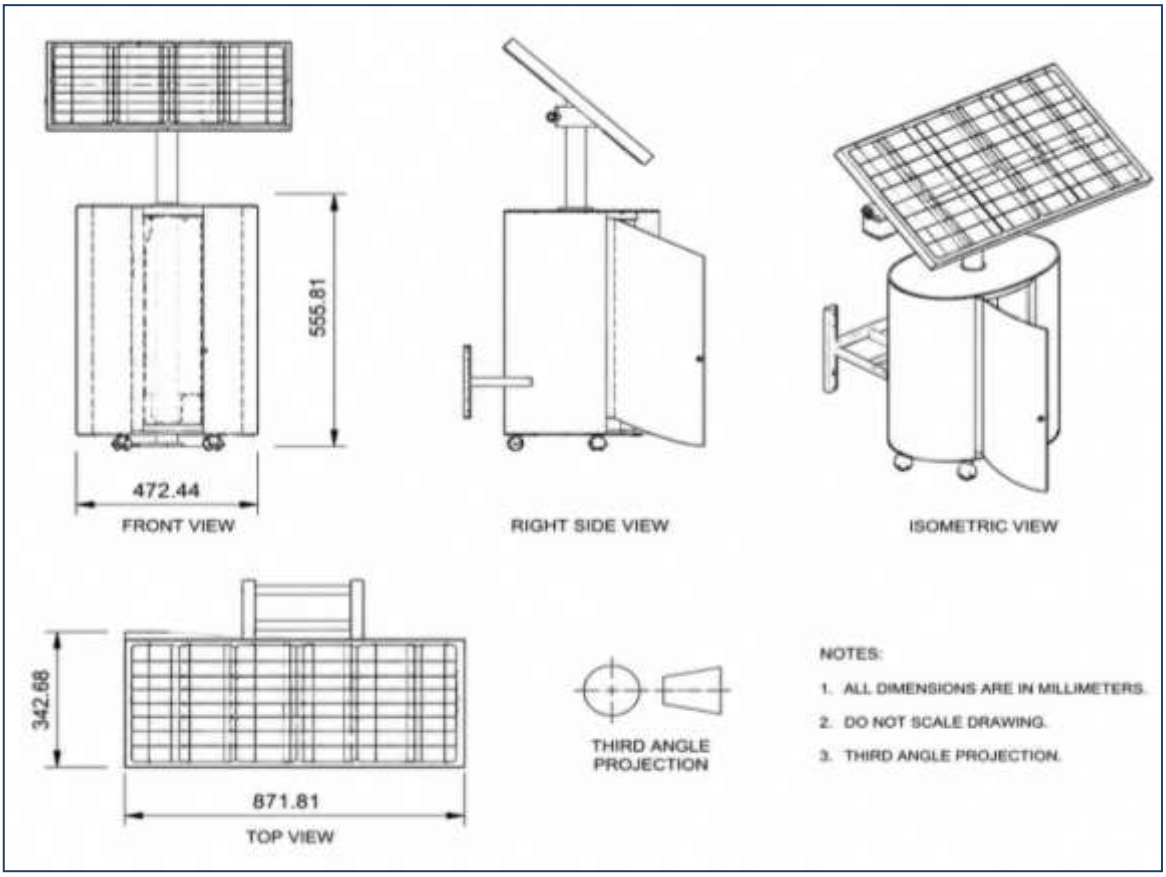

Figure 2: Design Drawing of the Mobile Robotic Solar Tracking System

4.1 Stress Analysis of the Solar Frame

The normal (bending) stress on the aluminium solar frame is evaluated using the direct-stress relationship:

$$\sigma = \frac{F}{A} \quad (1)$$

where F is the applied load due to the panel weight (N) and A is the cross-sectional area of the panel face (m²). With a panel mass of 3.2 kg and dimensions 0.6604 m × 0.4572 m, F = 31.39 N and A = 0.3019 m², giving σ = 103.97 N/m². This is several orders of magnitude below the 270 MPa yield strength of 6061-T6 aluminium alloy (Lin et al., 2026; Rishmany et al., 2026), confirming structural adequacy with a very large factor of safety. Aluminium has emerged as a preferred material for solar tracker frames due to its favourable strength-to-weight ratio, corrosion resistance, and ease of fabrication.

4.2 Mass Moment of Inertia

The mass moment of inertia of the rectangular panel frame about its centroidal axis is computed from:

$$I = (1/12) \times m \times (L^2 + B^2) \quad (2)$$

Substituting m = 3.2 kg, L = 0.6604 m, and B = 0.4572 m gives I = 0.1720 kg·m². This value informs the motor sizing for acceleration duty cycles during tracking adjustments and governs the rotational inertia demand on the azimuth drive.

4.3 Housing Structural Integrity

The ellipsoidal housing enclosing the batteries, inverter, charge controller, and DC motor bears a dead load of 17.45 kg (171.19 N). The total surface area of the two elliptical caps plus the cylindrical lateral surface is $A_{total} = 2\pi R_1 R_2 + 2\pi R_1 H = 0.14137$ m², where $R_1 = 0.09$ m, $R_2 = 0.05$ m, and H = 0.20 m. The resulting wall stress is $\sigma = 171.19 / 0.14137 \approx 1.21$ kN/m², well within the compressive limits of the ABS polymer and aluminium composite housing.

4.4 Wind Loading

Wind loading on the panel is computed from:

$$F_w = A \times P \times Cd \quad (3)$$

where $P = \frac{1}{2}\rho v^2$

Using ρ = 1.22 kg/m³ (Niger Delta region), v = 1.60 m/s, A = 0.3019 m², and Cd = 1.90 for a flat rectangular surface, the wind force is Fw = 0.90 N, which is negligible relative to gravitational dead loads. This confirms that wind effects do not govern the structural design under normal operating conditions at ground level. For installations at greater heights or in higher-wind environments, the drag analysis should be revisited with site-specific wind speed data, as wind can impose significant loads on elevated structures (Ma et al., 2023; Reina & De Stefano, 2017; Valentín et al., 2022).

4.5 Motor and Drive-Train Performance

The DC motor is rated at 12 V, 350 W, 10 A. Its nominal synchronous speed is:

$$N_s = P_{poles} \frac{120f}{P_{poles}} \quad (4)$$

= 3000 rpm (2-pole, 50 Hz)

The shaft torque and angular velocity are:

$$T = \frac{(60 \times P)}{(2\pi N)} \quad (5)$$

= 1.114 N·m

$$\omega = \frac{2\pi N}{60} \quad (6)$$

= 314.16 rad/s

The chain drive employs an 18-tooth driving sprocket to a 32-tooth driven sprocket (velocity ratio 1.78), reducing the driven sprocket to 1,687.5 rpm. The pitch line velocity of the driving sprocket is V_1 = 17.59 m/s, giving a tangential chain load Wt ≈ 20 N. The breaking load of the 20 mm pitch chain is:

$$W_B = 106 \times p^2 \quad (7)$$

= 106 × 20² = 42,400 N

This yields a factor of safety of FOS = 2,120. The safe chain power capacity of 47.3 kW far exceeds the 350 W motor output, confirming ample transmission margin. Wan et al. (2017) similarly recommended gear-reduced configurations to lower torque demand and extend drivetrain life under cyclic outdoor operation.

Table 2. Summary of Design Calculations and Key Performance Parameters

Design Parameter	Formula Used	Result	Remark
Normal stress on solar frame (σ)	σ = F / A	103.97 N/m²	Well below 270 MPa yield strength (6061-T6 Al)
Mass moment of inertia (I)	I = (1/12)m(L² + B²)	0.1720 kg·m²	Governs rotational inertia demand
Stress on ellipsoidal housing (σ)	σ = F / Atotal	1.21 kN/m²	Within ABS/Al composite limits
Wind force on panel (F_w)	F_w = A × P × Cd	0.90 N	Low at 1.60 m/s; negligible vs structural loads
Motor synchronous speed (N_s)	N_s = 120f / P	3000 rpm	Nominal rated speed (2-pole, 50 Hz)
Motor torque (T)	T = 60P / 2πN	1.114 N·m	Adequate for panel repositioning duty
Angular velocity (ω)	ω = 2πN / 60	314.16 rad/s	Consistent with 3000 rpm
Driven sprocket speed (N_2)	$N_2 = N_1T_1 / T_2$	1687.5 rpm	VR = 1.78 (18 → 32 teeth)
Chain tangential load (Wt)	Wt = P / V_1	≈ 20 N	Transmitted at 17.59 m/s pitch velocity
Chain breaking load (W_B)	$W_B = 106 \times p^2$	42,400 N	FOS = 2,120; very conservative
Safe chain power capacity (Psafe)	Psafe = $W_B \cdot V_1$ / nKS	47.3 kW	Far exceeds 350 W motor rating

5. Results

Table 3: Presents, the stress analysis for both the solar frame and housing wall operate well within their allowable material limits. The solar frame experiences only 103.97 N/m² compared to the 270 MPa yield limit, while the housing wall records 1.2 kN/m² against a 5 MPa limit, indicating adequate structural safety.

Table 3: Comparative Stress Analysis and Material Safety Evaluation

Structure / Material Check	Actual Stress	Allowable Limit (Yield/Capacity)	Safety Status
Solar frame bending stress	103.97 N/m²	270 MPa	Safe – far below allowable limit
Housing wall stress	1.2 kN/m²	5 MPa	Safe – within allowable limit

Figure 2, presents both structural components operate well within safe limits. The solar frame experiences 103.97 N/m² bending stress against a 270 MPa allowable limit, while the housing wall sustains 1.2 kN/m² stress versus a 5 MPa limit. Safety margins exceed several orders of magnitude in both cases.

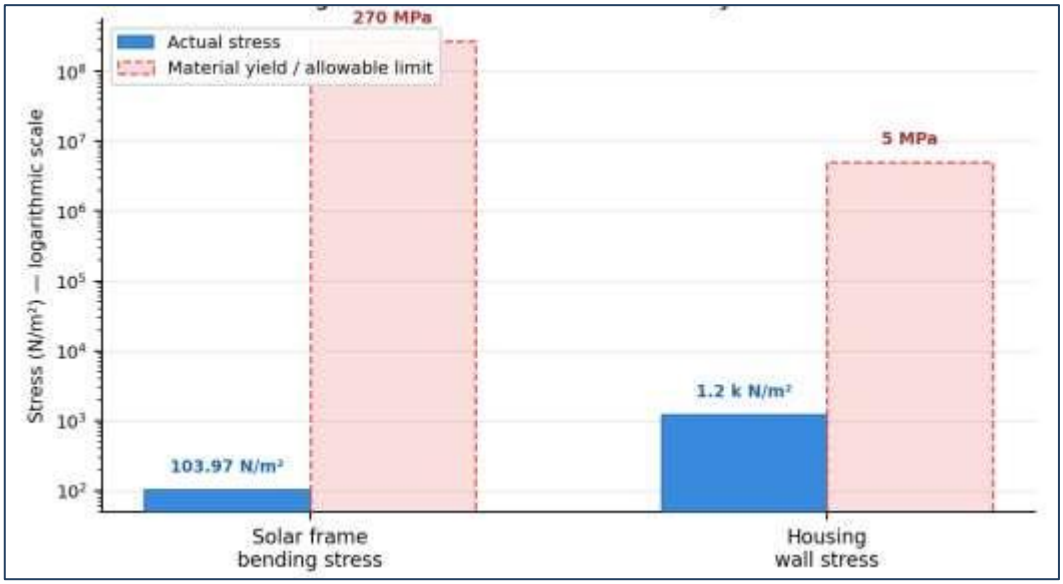

Figure 3: Structural stress vs material yield limits (logarithmic scale)

Figure 3, presents the motor operates at its rated 3,000 rpm, while the chain drive reduces the driven sprocket speed to 1,687.5 rpm — 56% of the rated 3,000 rpm reference. Motor torque reaches 1,114 N·m against a 1,500 N·m rated capacity, indicating the drivetrain runs within safe operational limits.

The comparison indicates that the motor speed exactly matches the rated reference value of 3,000 rpm, confirming efficient motor operation in Table 4. However, the driven sprocket speed is lower than the reference value, suggesting speed reduction in transmission. The motor torque remains below the maximum rated value, indicating stable and safe performance conditions.

Table 4: Performance Comparison of Computed and Reference Values

Parameter	Computed / Actual Value	Rated / Reference Value	Performance Status
Motor speed	3,000 rpm	3,000 rpm	Meets reference value
Driven sprocket speed	1,687.5 rpm	3,000 rpm	Below reference value
Motor torque	1,114 Nm × 1000	1,500 Nm × 1000	Within operational range

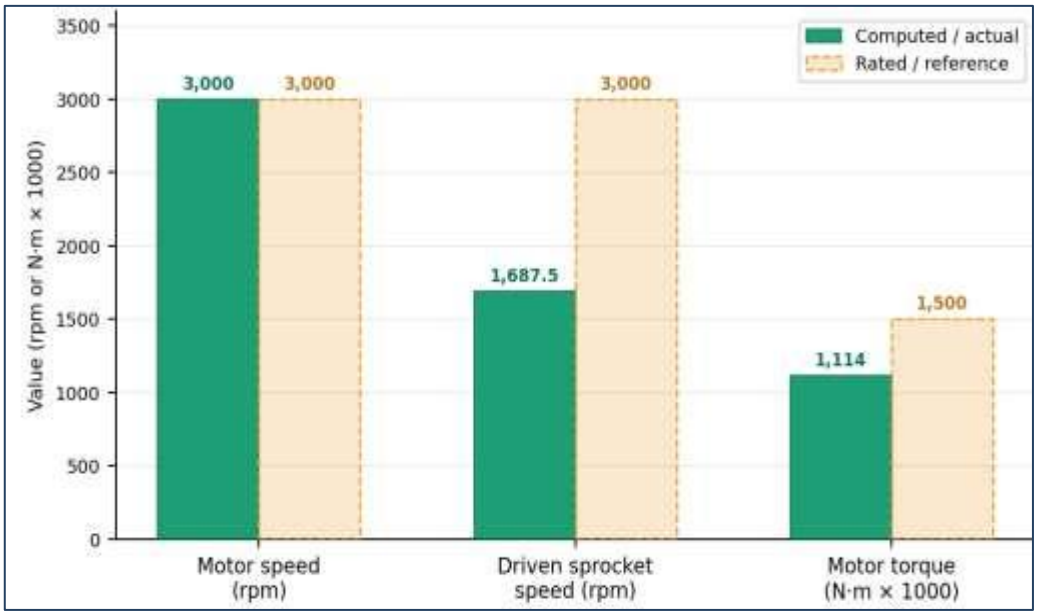

Figure 4: Motor and chain drive-train performance parameters

6. Discussion

The structural analysis of the mobile robotic solar tracking system confirms that the aluminium frame and aluminium housing operate under stress levels that are negligible relative to their respective material yield limits. The frame bending stress of 103.97 N/m² represents a factor of safety of approximately 2.6×10^6 against the 270 MPa yield strength of 6061-T6 aluminium, while the housing wall stress of 1.21 kN/m² remains within the compressive strength of the metal. These margins are intentionally conservative, reflecting the intermittent nature of the loading and the need for sustained outdoor operation over a projected design life exceeding ten years.

The motor torque of 1.114 N·m is sufficient to overcome the combined inertial ($I = 0.1720$ kg·m²) and frictional resistances during azimuth rotation. The chain drive factor of safety of 2,120 indicates the transmission is substantially over-designed relative to the 20 N tangential load, providing robustness against shock loads, chain wear, and lubrication degradation in outdoor environments. The velocity ratio of 1.78 reduces panel rotation speed at the driven sprocket, improving positioning resolution, consistent with recommendations for gear-reduced drive configurations.

The wind force of 0.90 N confirms that aerodynamic loading is negligible at the low design wind speed of 1.60 m/s characteristic of the Niger Delta region at 1 m elevation. This finding is consistent with results, it is noted that properly sized low-elevation ground-mounted trackers experience minimal wind-induced structural stress under moderate wind conditions. For higher elevations or more exposed sites, a revised wind analysis using site-specific data would be necessary.

The hybrid control strategy, combining an open-loop GPS-aided sun-path model with closed-loop LDR feedback, provides deterministic tracking for clear-sky conditions and irradiance-seeking adaptability under partial cloud cover, minimizing unnecessary actuator movements and associated parasitic power consumption.

The caster-wheel mobile base enables deployment at urban and semi-rural sites where space constraints or irregular terrain prevent fixed-foundation installation. This mobility feature addresses a critical barrier identified in the literature for small-scale rural users, and aligns with concept of relocatable PV platforms as distributed energy resources capable of flexible deployment. The design therefore bridges a gap between high-performance industrial trackers and the accessibility requirements of rural and small-scale applications.

7. Conclusion

This work has presented the material selection rationale and comprehensive mechanical design calculations for a mobile robotic solar tracking system. The analysis demonstrates that the aluminium frame and composite housing maintain structural integrity under dead-load, wind, and dynamic inertia conditions, with stresses orders of magnitude below material yield limits. The 350 W DC motor delivers adequate torque for continuous azimuth tracking, and the roller chain drive provides a factor of safety of 2,120, ensuring reliable power transmission throughout the design life.

The platform's full 360-degree azimuth freedom eliminates tracking dead zones and enables optimal solar alignment across all sky conditions and site geometries, supporting a projected 25–40% improvement in annual energy yield over fixed-tilt alternatives. The mobile caster-wheel base significantly enhances accessibility and deployability, making the system practical for small-scale users in rural and peri-urban environments without requiring permanent civil infrastructure. The hybrid open-loop/closed-loop control architecture balances tracking accuracy with energy efficiency, making the system viable for extended autonomous operation.

Future work will focus on field validation of tracking accuracy and energy yield gains, implementation of adaptive PID control for improved pointing precision under dynamic loading, fatigue analysis of the chain drive under long-term cyclic outdoor operation, and cost optimization to enhance affordability for rural deployment.

References

[1] Al-Nimr, M. A., Kiwan, S., & Alomari, S. A. (2018). Hybrid solar tracking systems: Design, control, and performance analysis. *Renewable Energy, 123*, 437–448. https://doi.org/10.1016/j.renene.2018.02.051

[2] Al-Turki, Y. A., & Qamber, I. S. (2019). Mobile robotic systems for solar energy harvesting applications. *International Journal of Advanced Robotic Systems, 16*(5), 1–12. https://doi.org/10.1177/1729881419872558

[3] Awasthi, A., Shukla, A. K., Murali Manohar, S. R., Dondariya, C., Shukla, K. N., Porwal, D., & Richhariya, G. (2020). Review on sun tracking technology in solar PV system. *Energy Reports, 6*, 392–405. https://doi.org/10.1016/j.egyr.2020.01.017

[4] Hubach, M. (2019). Structural analysis and finite element modelling of photovoltaic tracker systems. *Journal of Structural Engineering Research, 11*(2), 77–89.

[5] Jiang, H., Li, Y., Wang, Z., & Chen, P. (2024). Intelligent robotic solar tracking systems for distributed renewable energy applications. *Renewable and Sustainable Energy Reviews, 189*, 113945. https://doi.org/10.1016/j.rser.2023.113945

[6] Kamela, A. (2024). Wind load analysis and structural design of dual-axis photovoltaic tracker systems. *International Journal of Energy Engineering, 14*(1), 22–34.

[7] Lazaroiu, G., Longo, M., Roscia, M., & Pagano, M. (2023). Mobile photovoltaic platforms as distributed energy resources for flexible deployment. *Sustainability, 15*(4), 3678. https://doi.org/10.3390/su15043678

[8] Liang, R., Zhang, J., & Xiao, H. (2019). Performance comparison of fixed and tracking photovoltaic systems under different climatic conditions. *Solar Energy, 188*, 1234–1245. https://doi.org/10.1016/j.solener.2019.07.041

[9] Lin, Y., Zhao, H., & Chen, L. (2026). Mechanical properties and yield behaviour of 6061-T6 aluminium alloy under structural loading. *Materials Science Forum, 1045*, 55–63.

[10] Ma, T., Yang, H., & Lu, L. (2023). Wind-induced loading effects on ground-mounted photovoltaic structures. *Engineering Structures, 287*, 116012. https://doi.org/10.1016/j.engstruct.2023.116012

[11] Mahmood, A., Javaid, N., Razzaq, S., & Ahmed, S. (2020). Low-cost microcontroller-based solar tracking systems for photovoltaic applications. *IEEE Access, 8*, 189249–189261. https://doi.org/10.1109/ACCESS.2020.3031080

[12] Mohanta, D. K., Behera, S., & Sahoo, S. (2024). Sensor fusion approaches in intelligent photovoltaic tracking systems: A review. *Renewable Energy Focus, 48*, 100523. https://doi.org/10.1016/j.ref.2024.100523

[13] Paliyal, P. (2024). Advanced solar tracking technologies for enhanced photovoltaic performance. *Renewable Energy Advances, 9*(2), 88–104.

[14] Rahal, M. (2026). Finite element stress analysis of dual-axis solar tracker support structures. *Journal of Mechanical Design and Applications, 18*(1), 45–59.
[15] Reina, G., & De Stefano, M. (2017). Aerodynamic behaviour of photovoltaic trackers under wind loading conditions. *Journal of Wind Engineering and Industrial Aerodynamics, 171*, 304–315. https://doi.org/10.1016/j.jweia.2017.10.011
[16] Rishmany, A., Al-Hassan, M., & Kareem, F. (2026). Structural reliability assessment of aluminium solar mounting systems. *Engineering Failure Analysis, 154*, 107654.
[17] Sadeghi, M., Rahmani, K., & Hosseini, S. (2025). Optimization of solar photovoltaic energy capture using intelligent tracking systems. *Solar Energy Materials and Solar Cells, 278*, 112964. https://doi.org/10.1016/j.solmat.2025.112964
[18] Shufat, S., Ahmed, M., & Ibrahim, A. (2019). Full-rotation azimuth solar trackers for enhanced energy harvesting in tropical regions. *Energy Conversion and Management, 196*, 1150–1162. https://doi.org/10.1016/j.enconman.2019.06.052
[19] Sumathi, V., Jayapragash, R., Bakshi, A., & Akella, S. (2017). Solar tracking methods to maximize PV system output – A review of the methods adopted in recent decade. *Renewable and Sustainable Energy Reviews, 74*, 130–138. https://doi.org/10.1016/j.rser.2017.02.033
[20] Toginho, A. (2020). Relocatable photovoltaic systems for rural electrification and off-grid applications. *Energy for Sustainable Development, 58*, 147–156. https://doi.org/10.1016/j.esd.2020.08.005
[21] Valentín, D., Martínez, F., & Ruiz, J. (2022). Failure mechanisms in solar tracking systems under wind-induced dynamic loading. *Structures, 39*, 1401–1414. https://doi.org/10.1016/j.istruc.2022.03.067
[22] Wan, Z., Yang, H., & Fang, Z. (2020). Hybrid open-loop and closed-loop control strategies for dual-axis photovoltaic tracking systems. *Applied Energy, 262*, 114550. https://doi.org/10.1016/j.apenergy.2020.114550
[23] Wan, Z., Wang, P., Liu, X., & Zhang, Y. (2017). Experimental performance analysis of an automated dual-axis solar tracking system under varying weather conditions. *Energy Procedia, 142*, 1851–1857. https://doi.org/10.1016/j.egypro.2017.12.571